Journal of Sound and Vibration 329 (2010) 1760–1779

Contents lists available at ScienceDirect

Journal of Sound and Vibration

journal homepage: www.elsevier.com/locate/jsvi

Experimental and numerical study on damage detection in an L-joint using guided wave propagation

Magdalena Rucka *

Department of Structural Mechanics and Bridge Structures, Faculty of Civil and Environmental Engineering, Gdansk University of Technology, ul. Narutowicza 11/12, 80-233 Gdańsk, Poland

ARTICLE INFO

Article history:
Received 14 May 2009
Received in revised form
27 November 2009
Accepted 3 December 2009
Handling Editor: A.V. Metrikine
Available online 30 December 2009

ABSTRACT

Longitudinal and flexural wave propagation in a steel L-joint is considered in this paper. Particular attention is paid to damage detection aspects. Experimental investigations were conducted on an intact L-joint as well as on an L-joint with a notch. Velocity time histories of elastic waves propagation have been applied to find the location of damage. To model longitudinal as well as flexural wave propagation including lateral and shear deformations, the special frame spectral element in the time domain, based on the Mindlin–Herrmann rod and Timoshenko beam theories, was formulated. As a result this paper discusses in detail the possibility of detection of damage in an L-joint and it compares the usefulness of the application of axial and flexural waves in non-destructive damage detection for this typical structural component.

1. Introduction

Guided wave-based damage detection methods have been intensively developed over last years and have attracted many researchers' interest. The guided wave propagation technique utilizes an excitation of very high frequencies in the form of an impulse or a wave packet. In the wave propagation approach, a structure can be perceived as a waveguide, which directs the wave energy along its length. Guided ultrasonic waves are very attractive due to their ability of inspecting large structures over long distances with a small number of transducers. This idea has been followed by many research groups, and it is used with success in some practical applications [1,2]; especially for plates [3,4], pipes [4,5], rails [6,7], or aircraft structures [8,9].

Modelling of wave propagation phenomena is possible in both time and frequency domains. One of frequency based methods is the spectral finite element method (SFEM) developed by Doyle [10]. The SFEM has been widely extended by Gopalakrishnan et al. [11] to anisotropic media. Numerical analysis of wave propagation by the SFEM in an isotropic cracked rod, a Timoshenko beam and a plate can be found in Refs. [12–14]. A numerical study on wave propagation in a rigid angle joint with three composite members is presented in Ref. [15]. To overcome drawbacks of the conventional Fourier-based SFEM connected with the required assumption of periodicity, Mitra and Gopalakrishnan proposed the use of the wavelet transform [16,17], instead of the Fourier transform. Igawa et al. [18] applied the Laplace transform to avoid the problem of periodicity, which made an analysis of a frame of arbitrary geometry based on the Euler–Bernoulli theory possible. Modelling of wave propagation can also be performed by the finite element method (FEM), e.g. [19]. The advantage of this approach is the availability of numerous commercial FEM codes and its great ability to solve problems

* Tel.: +48 58 347 24 97; fax: +48 58 347 16 70.
E-mail address: mrucka@pg.gda.pl

0022-460X/$ - see front matter © 2009 Elsevier Ltd. All rights reserved.
doi:10.1016/j.jsv.2009.12.004

involving complicated geometry [20]. However, the application of the FEM to wave propagation modelling requires very fine mesh, i.e. it is recommended to use more than 20 nodes per wavelength [19]. A different approach is offered by the time domain spectral element method (SEM) developed by Patera [21]. This method is an expansion of the FEM and it has the same view-point as the *p*-version of the finite element method. The main idea of the SEM is the use of an interpolating polynomial of high degree. In the SEM, Lagrange polynomials are applied at Gauss-Legendre-Lobbatto nodes [22]. The spectral element method can also be based on Chebyshev polynomials as basis functions at Chebyshev–Gauss–Lobatto points [23]. In the comparison with the FEM, the SEM brings two important benefits. First of all, when spectral elements are used, the required number of nodes per wavelength is of order of 10 or less. In addition, in the SEM approach the element matrices are integrated using the Gauss-Legendre-Lobbatto quadrature so that the local element mass matrix is of diagonal structure, what enables efficient numerical temporal integration. Spectral elements in the time domain are available for a rod based on the elementary theory [24], a Timoshenko beam [24], a membrane [25] and a plate [26]. An analysis of wave propagation in three-dimensional (3D) truss structures is given in Ref. [27]. Recently, Peng et al. [28] have presented interesting study on the application of the 3D spectral element method to wave propagation problems in plate structures, discussing the aspect of damage detection.

Complications met in investigations of wave propagation in complex structural systems suggest careful studies of simpler structural elements. Such the element is a joint of two straight rods, called an L-joint. The L-joint can also be a component of more complex engineering structures or it can represent the simplest frame structure. The analysis of wave propagation in an L-joint is of practical interest due to the mode conversion. An incident wave of one type, after reaching a junction generates propagation and reflection of waves of other types, what causes damage detection more difficult than for a simple rod. The earliest studies concerned analytical models of longitudinal as well as flexural wave propagation at a junction of two non-collinear rods [29]. Lee and Kolsky [29] used the elementary rod theory to describe propagation of longitudinal waves and the Timoshenko beam theory for flexural wave propagation. In experiments, a bent steel rod was used. Strain gages were attached to the specimen and an incident pulse was created by firing a projectile, so that axial impact was achieved. Atkins and Hunter [30] presented an analytical model of wave propagation in an L-type joint. In performed experimental investigations a longitudinal pulse was induced by a projectile, whereas strains were measured by strain gauges. Liang and Chen [31] studied theoretically reflection and transmission of longitudinal waves around a right-angled joint of two rods. They concluded that when a horizontal rod of an L-joint was applied a force along its length, a longitudinal wave through a welded joint nearly cannot transmit into a vertical rod. Beccu et al. [32] studied longitudinal elastic waves in a bent bar. Experiments were performed on a bar with a sharp bend as well as with a smooth bend. Bars were impacted axially by a cylindrical carbon steel piston accelerated by an air gun and strain gages were applied to monitor strains. Numerical simulations of wave propagation in an L-joint using the SFEM were initiated by Doyle and Farris [33]. They developed a spectrally formulated element for wave propagation in frame structures based on the elementary rod theory and the Euler–Bernoulli beam theory. This model was examined on an L-joint consisting of two semi-infinite members. To respect dispersion, modified rod theories were formulated in the frequency domain approach. Martin et al. [34] formulated a frame element by combining the Mindlin–Herrmann rod with the Timoshenko beam in the frequency domain. Numerical simulations have been conducted on two semi-infinite rods connected with a 45° joint. However, these modified theories have not been compared with experimental results. Moreover, the above mentioned experimental and numerical studies were performed for non-damaged L-joints only.

This paper is devoted to wave propagation in form of a wave packet in a steel L-type joint. Such the connection of two rods can be found in many structural elements of civil and mechanical engineering, yet it is not well addressed in the literature of structural health monitoring (SHM). The purpose of this study is to investigate numerically and experimentally particular problems of longitudinal and flexural wave propagation for the L-joint structural element. To model longitudinal as well as flexural wave propagation taking lateral deformations and shear deformations into consideration, the special frame spectral element, based on the Mindlin–Herrmann rod and the Timoshenko beam theories was formulated in the time domain. Particular attention was paid to damage detection in the L-joint. As a result, this paper discusses in detail the possibility of detection of damage in the L-joint and compares the usefulness of axial and flexural waves in non-destructive damage detection.

2. Formulation of spectral element method for a plane frame

2.1. Mindlin–Herrmann rod theory

The elementary wave theory for a thin rod (cf. [10]) assumes the presence of one-dimensional uniform axial stress only. It also neglects the lateral contraction and the result of the governing wave equation is a non-dispersive signal. An improvement of the elementary one-mode rod theory can be achieved by taking into consideration effects of the lateral inertia. A rod deforms not only in longitudinal direction, but it also contracts due to the Poisson's ratio effect. The Mindlin–Herrmann theory [35] introduces the lateral contraction $\psi(x,t)$, which is assumed to be independent of the axial deformation $u(x,t)$. Displacements in deep rod theory are approximated by:

$$\overline{u}(x,y) \approx u(x), \quad \overline{v}(x,y) \approx \psi(x)y. \tag{1}$$

The governing equations for the Mindlin–Herrmann rod are:

$$\frac{2GA}{1-\nu}\left[\frac{\partial^2 u}{\partial x^2}+\nu\frac{\partial \psi}{\partial x}\right]=\rho A\ddot{u}-f(x,t),\quad K_1^{M-H}GI\frac{\partial^2\psi}{\partial x^2}-\frac{2GA}{1-\nu}\left[\nu\frac{\partial u}{\partial x}+\psi\right]=K_2^{M-H}\rho I\ddot{\psi}, \tag{2}$$

where $f(x,t)$ is the external force, t and x denote temporal and spatial variables, respectively. Material and geometrical parameters: the modulus of elasticity, the shear modulus, the Poisson's ratio, the mass density, the cross-section and the moment of inertia are denoted by E, G, ν, ρ, A, and I, respectively. The kinetic T and the strain energy U are formulated as follows:

$$T=\frac{1}{2}\int_L(\rho A\dot{u}^2+K_2^{M-H}\rho I\dot{\psi}^2)\,\mathrm{d}x \tag{3}$$

$$U=\frac{1}{2}\int_L\left\{\frac{EA}{1-\nu^2}\left[\left(\frac{\partial u}{\partial x}\right)^2+\psi^2+2\nu\frac{\partial u}{\partial x}\psi\right]+K_1^{M-H}GI\left(\frac{\partial\psi}{\partial x}\right)^2\right\}\mathrm{d}x \tag{4}$$

Constants K_1^{M-H} and K_2^{M-H} are adjustable parameters to compensate for the approximation of displacement fields given by Eq. (1). The choice of values of parameters K_1^{M-H} and K_2^{M-H} affects the value of the group velocity. Different rules to establish parameters K_1^{M-H} and K_2^{M-H} are considered in Refs. [10] and [34]. Marin et al. [34] proposed to select K_1^{M-H} and K_2^{M-H} based upon comparison with 2-D finite element results. In this study, in which experimental investigations are reported, the parameters $K_1^{M-H}=1.1$ and $K_2^{M-H}=2.1$ are chosen to give the best fit to experimentally measured wave velocity for the considered frequency range. An axial propagating wave in a rod was measured for the frequency 100 and 120 kHz, and the parameters K_1^{M-H} and K_2^{M-H} were determined by the method of least squares.

2.2. Timoshenko beam theory

The Timoshenko beam theory takes into account the effect of shear deformation. The displacement field is approximated by two independent functions $\varphi(x)$ and $v(x)$:

$$\overline{u}(x,t)\approx -y\varphi(x),\quad \overline{v}(x,t)\approx v(x). \tag{5}$$

The Timoshenko governing equations for flexural motion of a beam are formulated as [10]:

$$K_1^{\mathrm{Tim}}GA\frac{\partial}{\partial x}\left(\frac{\partial v}{\partial x}-\varphi\right)=\rho A\ddot{v}-f(x,t),\quad EI\frac{\partial^2\varphi}{\partial x^2}+K_1^{\mathrm{Tim}}GA\left(\frac{\partial v}{\partial x}-\varphi\right)=K_2^{\mathrm{Tim}}\rho I\ddot{\varphi}. \tag{6}$$

The kinetic T and the strain energy U become:

$$T=\frac{1}{2}\int_L(\rho A\dot{v}^2+K_2^{\mathrm{Tim}}\rho I\dot{\varphi}^2)\,\mathrm{d}x,\quad U=\frac{1}{2}\int_L\left\{EI\left(\frac{\partial\varphi}{\partial x}\right)^2+K_1^{\mathrm{Tim}}GA\left(\frac{\partial v}{\partial x}-\varphi\right)^2\right\}\mathrm{d}x, \tag{7}$$

where $v(x,t)$ is the vertical displacement, $\varphi(x,t)$ is the rotation, $f(x,t)$ is the external force, t and x denote temporal and spatial variables, respectively. Material and geometrical parameters: the modulus of elasticity, the shear modulus, the mass density, the cross-section and the moment of inertia are denoted by E, G, ρ, A and I, respectively. Constants K_1^{Tim} and K_2^{Tim} are adjustable parameters. There are different rules to establish parameters K_1^{Tim} and K_2^{Tim} [10]. In this study the parameter $K_1^{\mathrm{Tim}}=0.95$ is chosen to give the best fit to experimentally measured wave velocity for the considered frequency range and K_2^{Tim} is equal to $12K_1^{\mathrm{Tim}}/\pi^2$ to match the cut-off frequency with Lamb modes. A flexural propagating wave in a rod was measured for the frequency 100 and 120 kHz, and the parameter K_1^{Tim} was determined by the method of least squares.

2.3. Spectral element formulation

The *M-H-Tim* frame element consists of the Mindlin–Herrmann rod (*M–H*) combined with the Timoshenko beam (*Tim*). Strains in the frame element can be written as:

$$\boldsymbol{\varepsilon}(x,t)=\begin{Bmatrix}\boldsymbol{\varepsilon}^{M-H}\\ \boldsymbol{\varepsilon}^{\mathrm{Tim}}\end{Bmatrix}=\begin{bmatrix}\mathbf{D}^{M-H} & \mathbf{0}\\ \mathbf{0} & \mathbf{D}^{\mathrm{Tim}}\end{bmatrix}\begin{Bmatrix}\mathbf{u}^{M-H}\\ \mathbf{v}^{\mathrm{Tim}}\end{Bmatrix}=\mathbf{D}\mathbf{q}(x,t), \tag{8}$$

where:

$$\boldsymbol{\varepsilon}^{M-H}=\begin{Bmatrix}u_{,x}\\ \psi\\ \psi_{,x}\end{Bmatrix},\quad \boldsymbol{\varepsilon}^{\mathrm{Tim}}=\begin{Bmatrix}v_{,x}-\varphi\\ \varphi_{,x}\end{Bmatrix},\quad \mathbf{D}^{M-H}=\begin{bmatrix}\frac{\partial}{\partial x} & 0\\ 0 & 1\\ 0 & \frac{\partial}{\partial x}\end{bmatrix},\quad \mathbf{D}^{\mathrm{Tim}}=\begin{bmatrix}\frac{\partial}{\partial x} & -1\\ 0 & \frac{\partial}{\partial x}\end{bmatrix}. \tag{9}$$

Following classical steps, the weak formulation is obtained in the form:

$$\int_L \delta\mathbf{q}^T\boldsymbol{\mu}\ddot{\mathbf{q}}\,\mathrm{d}x+\int_L \delta\boldsymbol{\varepsilon}^T\mathbf{E}\boldsymbol{\varepsilon}\,\mathrm{d}x=\int_L \delta\mathbf{q}^T\mathbf{f}\,\mathrm{d}x, \tag{10}$$

where the stress–strain matrix $\mathbf{E}$ and mass density matrix $\boldsymbol{\mu}$ are defined as follows:

$$\mathbf{E}=\begin{bmatrix}\mathbf{E}^{M-H} & \mathbf{0}\\ \mathbf{0} & \mathbf{E}^{\mathrm{Tim}}\end{bmatrix},\quad \boldsymbol{\mu}=\begin{bmatrix}\boldsymbol{\mu}^{M-H} & \mathbf{0}\\ \mathbf{0} & \boldsymbol{\mu}^{\mathrm{Tim}}\end{bmatrix}, \tag{11}$$

$$\mathbf{E}^{M-H}=\begin{bmatrix}\dfrac{EA}{1-\nu^2} & \dfrac{\nu EA}{1-\nu^2} & 0\\ \dfrac{\nu EA}{1-\nu^2} & \dfrac{EA}{1-\nu^2} & 0\\ 0 & 0 & K_1^{M-H}GI\end{bmatrix},\quad \boldsymbol{\mu}^{M-H}=\begin{bmatrix}\rho A & 0\\ 0 & K_2^{M-H}\rho I\end{bmatrix}, \tag{12}$$

$$\mathbf{E}^{\mathrm{Tim}}=\begin{bmatrix}K_1^{\mathrm{Tim}}GA & 0\\ 0 & EI\end{bmatrix},\quad \boldsymbol{\mu}^{\mathrm{Tim}}=\begin{bmatrix}\rho A & 0\\ 0 & K_2^{\mathrm{Tim}}\rho I\end{bmatrix}. \tag{13}$$

For standard C^0 elements [36,37], interpolation of the displacement field $\mathbf{q}(\xi,t)$ in an element of length $L_{(e)}$ becomes:

$$\tilde{\mathbf{q}}(\xi,t)=\begin{Bmatrix}\tilde{u}(\xi,t)\\ \tilde{\psi}(\xi,t)\\ \tilde{v}(\xi,t)\\ \tilde{\varphi}(\xi,t)\end{Bmatrix}=\mathbf{N}_{(e)}(\xi)\mathbf{q}_{(e)}(t),\quad \mathbf{N}_{(e)}(\xi)=[\mathbf{N}_1(\xi)\mathbf{N}_2(\xi)\ldots\mathbf{N}_n(\xi)],\quad \mathbf{q}_{(e)}(t)=\begin{Bmatrix}\mathbf{q}_1(t)\\ \mathbf{q}_2(t)\\ \vdots\\ \mathbf{q}_n(t)\end{Bmatrix}, \tag{14}$$

$$\mathbf{N}_i(\xi)=\begin{bmatrix}N_i(\xi) & 0 & 0 & 0\\ 0 & N_i(\xi) & 0 & 0\\ 0 & 0 & N_i(\xi) & 0\\ 0 & 0 & 0 & N_i(\xi)\end{bmatrix},\quad \mathbf{q}_i(t)=\begin{Bmatrix}u_i(t)\\ \psi_i(t)\\ \nu_i(t)\\ \varphi_i(t)\end{Bmatrix},\quad i=1,2,\ldots,n, \tag{15}$$

where tilde denotes the approximated quantity, n is the number of element nodes, N_i are interpolation polynomials of order $n-1$, $\xi\in[-1,+1]$ is the parent domain and label $(.)_i$ denotes nodal values. Strains in the *M-H-Tim* element can be interpolated through the relation:

$$\tilde{\boldsymbol{\varepsilon}}(\xi,t)=\mathbf{B}_{(e)}(\xi)\mathbf{q}_{(e)}(t), \tag{16}$$

where the strain-displacement operator and the Jacobian are given by the following relations:

$$\mathbf{B}_{(e)}(\xi)=\tilde{\mathbf{D}}\mathbf{N}_{(e)}(\xi),\quad \tilde{\mathbf{D}}=\begin{bmatrix}\tilde{\mathbf{D}}^{M-H} & \mathbf{0}\\ \mathbf{0} & \tilde{\mathbf{D}}^{\mathrm{Tim}}\end{bmatrix},\quad \frac{\partial}{\partial x}=j^{-1}\frac{\partial}{\partial\xi}, \tag{17}$$

$$\tilde{\mathbf{D}}^{M-H}=\begin{bmatrix}\dfrac{1}{j}\dfrac{\partial}{\partial\xi} & 0\\ 0 & 1\\ 0 & \dfrac{1}{j}\dfrac{\partial}{\partial\xi}\end{bmatrix},\quad \tilde{\mathbf{D}}^{\mathrm{Tim}}=\begin{bmatrix}\dfrac{1}{j}\dfrac{\partial}{\partial\xi} & -1\\ 0 & \dfrac{1}{j}\dfrac{\partial}{\partial\xi}\end{bmatrix}. \tag{18}$$

Substitution of Eqs. (14) and (16) into (10) provides that following set of equations holds on the local element level:

$$\mathbf{M}_{(e)}\ddot{\mathbf{q}}_{(e)}+\mathbf{K}_{(e)}\mathbf{q}_{(e)}=\mathbf{f}_{(e)}, \tag{19}$$

where $\mathbf{K}_{(e)}$ and $\mathbf{M}_{(e)}$ are element matrices, $\mathbf{f}_{(e)}$ denotes the vector of element applied forces. To evaluate element matrices, a numerical integration is employed. Element matrices are integrated using the Gauss-Lobatto-Legendre (GLL) quadrature. Therefore, formulae for the stiffness matrix, the mass matrix and the load vector become:

$$\mathbf{K}_{(e)}=\sum_{p=1}^{n_p} w_p\mathbf{B}_{(e)}^T(\xi_p)\mathbf{E}\mathbf{B}_{(e)}(\xi_p)j(\xi_p), \tag{20}$$

$$\mathbf{M}_{(e)}=\sum_{p=1}^{n_p} w_p\mathbf{N}_{(e)}^T(\xi_p)\boldsymbol{\mu}\mathbf{N}_{(e)}(\xi_p)j(\xi_p), \tag{21}$$

$$\mathbf{f}_{(e)}=\sum_{p=1}^{n_p} w_p\mathbf{N}_{(e)}^T(\xi_p)\mathbf{f}_{(e)}(\xi_p)j(\xi_p), \tag{22}$$

where n_p is the number of integration points, $p \in 1,2,\ldots,n_p$ is the label of ξ_p i.e. abscissa and w_p are corresponding weights. The coordinates of the Gauss-Lobatto-Legendre (GLL) integration points ξ_p are obtained as the roots of the equation [22]:

$$(1-\xi^2)\frac{\mathrm{d}P_{n_p-1}(\xi)}{\mathrm{d}\xi}=0, \tag{23}$$

where P_{n_p-1} denotes the Legendre polynomial of degree (n_p-1) and the associated weights w_p of the points ξ_p are:

$$w_p=\frac{2}{n_p(n_p-1)(P_{n_p-1}(\xi_p))^2}. \tag{24}$$

In the GLL integration, the coordinates ξ_p determine the location of finite element nodes, called GLL nodes. These are the nodes for Lagrange polynomials N_i in the parent domain $[-1,+1]$. Due to the Gauss-Lobatto-Legendre rule, interpolation carried out over the GLL nodes leads to the diagonal local mass matrix:

$$\mathbf{M}_{(e)}=\begin{bmatrix}\mathbf{M}_1 & \mathbf{0} & \cdots & \mathbf{0}\\ \mathbf{0} & \mathbf{M}_2 & \cdots & \mathbf{0}\\ \vdots & \vdots & \ddots & \vdots\\ \mathbf{0} & \mathbf{0} & \cdots & \mathbf{M}_n\end{bmatrix},\quad \mathbf{M}_p=\begin{bmatrix}\rho A & 0 & 0 & 0\\ 0 & K_2^{M-H}\rho I & 0 & 0\\ 0 & 0 & \rho A & 0\\ 0 & 0 & 0 & K_2^{\mathrm{Tim}}\rho I\end{bmatrix}w_p j(\xi_p), \tag{25}$$

according to the properties $N_i(\xi_p)=\delta_{ip}$ of shape functions and $N_i(\xi_p)N_j(\xi_p)=\delta_{ip}\delta_{jp}$, $i,j,p=1,2,\ldots,n_p\equiv n$.

The above developed element is transformed to the global coordinate system. The transformation matrix enables rotation of local axes to structural axes:

$$\mathbf{T}_{(e)}=\begin{bmatrix}\mathbf{T}_1 & \mathbf{0} & \mathbf{0} & \mathbf{0}\\ \mathbf{0} & \mathbf{T}_2 & \mathbf{0} & \mathbf{0}\\ \mathbf{0} & \mathbf{0} & \ldots & \mathbf{0}\\ \mathbf{0} & \mathbf{0} & \mathbf{0} & \mathbf{T}_n\end{bmatrix},\quad \mathbf{T}_{(i)}=\begin{bmatrix}\cos\alpha & 0 & \sin\alpha & 0\\ 0 & 1 & 0 & 0\\ -\sin\alpha & 0 & \cos\alpha & 0\\ 0 & 0 & 0 & 1\end{bmatrix}. \tag{26}$$

The transformation of local element matrices to global matrices is given by:

$$\overline{\mathbf{K}}_{(e)}=\mathbf{T}_{(e)}^T\mathbf{K}_{(e)}\mathbf{T}_{(e)},\quad \overline{\mathbf{M}}_{(e)}=\mathbf{T}_{(e)}^T\mathbf{M}_{(e)}\mathbf{T}_{(e)},\quad \overline{\mathbf{f}}_{(e)}=\mathbf{T}_{(e)}^T\mathbf{f}_{(e)}. \tag{27}$$

Then the system of equations of motion is built in the course of standard aggregation of element matrices and vectors referred to the structural coordinate system:

$$\mathbf{K}=A_{e=1}^{N_{\mathrm{element}}}\overline{\mathbf{K}}_{(e)},\quad \mathbf{M}=A_{e=1}^{N_{\mathrm{element}}}\overline{\mathbf{M}}_{(e)},\quad \mathbf{f}=A_{e=1}^{N_{\mathrm{element}}}\overline{\mathbf{f}}_{(e)}. \tag{28}$$

3. Experimental setup

Wave propagation experiments were performed on a steel L-type joint as well as on a steel rod (Fig. 1). The rod has length $L=1000$ mm and cross-section 6 mm × 6 mm. The L-joint was prepared through a welding process. It consists of two rods of cross-section 6 mm × 6 mm and length $L=995$ mm measured between axes, as shown in Fig. 1c. The rods were chamfered at 45° and joined in the L-joint corner with a butt weld. Then the weld was ground to obtain the origin cross-section (Fig. 1c, d). The experimentally determined mass density ρ is equal to 7556 kg/m^3. The modulus of elasticity was also determined experimentally in a force-displacement test (tensile test) using a strain gauge attached to the rod in the longitudinal direction and a testing machine to register a force level, and its value equals $E=200.11$ GPa. The Poisson's ratio ν was set at 0.33. The L-joint specimen is shown in Fig. 2a. It had free-free boundary conditions and there was no fixture, which could affect wave propagation. Since excited waves had very low amplitudes, no rigid movement occurred. Four specimens have been taken into investigations, namely the intact rod, the intact L-joint, the rod with a notch and the L-joint with a notch. The rectangular notch with dimensions 2 mm in length and 1 mm in height was obtained by a precision cut. The depth of the notch equals 16.7 percent of the rod height. The notch was introduced at the distance $L_r=0.5L$ from the left edge of the specimen (Fig. 1b, d).

The photo of the experimental setup is presented in Fig. 2a. To excite waves the piezoelectric (PZT) plate actuator Noliac CMAP11 was applied. The actuator of dimensions 5 mm × 5 mm × 2 mm was bonded at one end of the specimen to excite axial and flexural waves, as it is shown in Fig. 2b and c, respectively. The Tektronix function generator with the amplifier creates an excitation signal. A propagating velocity signal was detected and registered on the opposite end of the specimen by the scanning head PSV-I-400 of the Polytec Scanning Laser Vibrometer PSV-3D-400-M using the VD-07 velocity decoder. As an excitation, a twelve-peak sinusoidal signal modulated by a Hanning window was chosen. The Hanning window provided smoothed tone burst in order to reduce excitation of side frequencies [1]. The application of a 12-count burst ensured relatively narrow spectrum what enabled reduction of the problem of dispersion. In both the rod and the L-joint specimens, longitudinal as well as flexural waves were excited and measured. In the case of longitudinal waves, the signal of frequency 120 kHz was excited, whereas in the case of flexural waves, the frequency of signal was 100 kHz. These frequencies were found to be more effective in considered specimens and applied instrumentation.

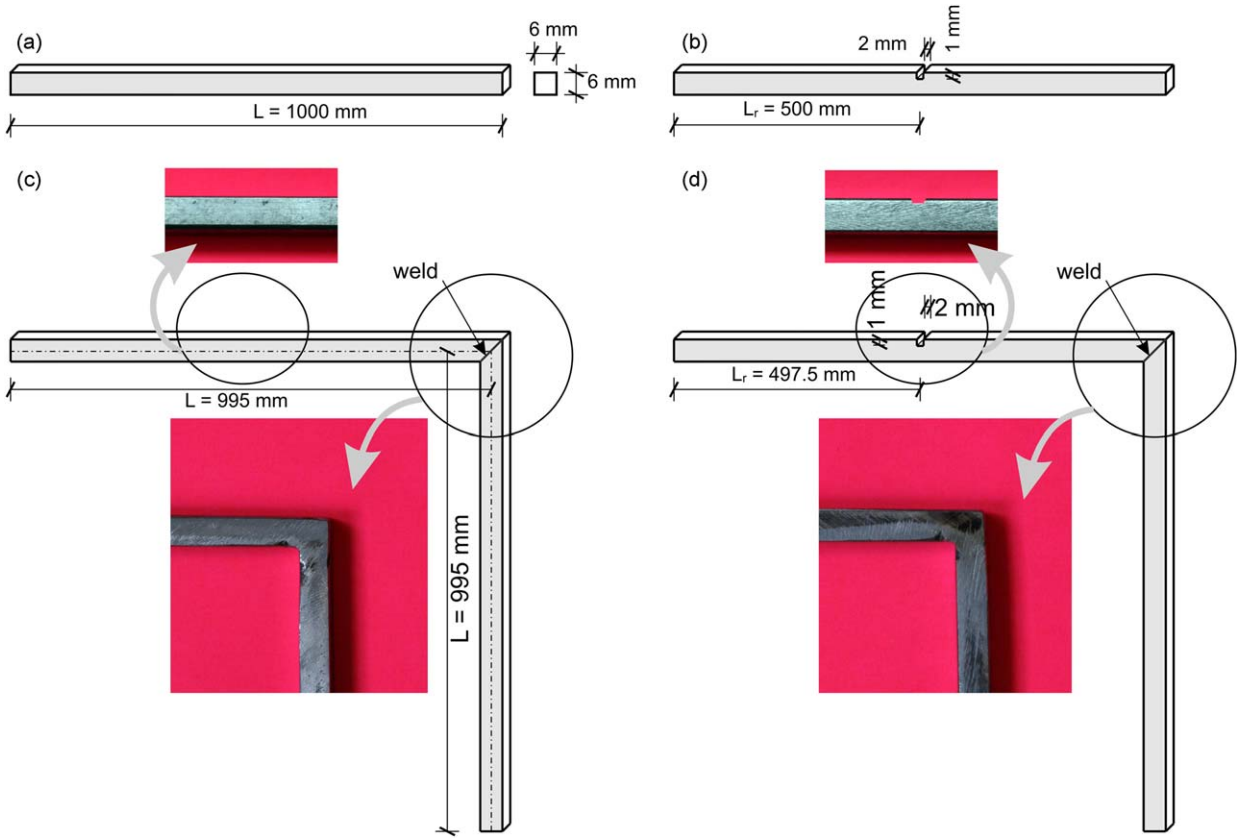

Fig. 1. Geometry of experimentally tested specimens: (a) ideal rod; (b) rod with the notch; (c) ideal L-joint; (d) L-joint with the notch.

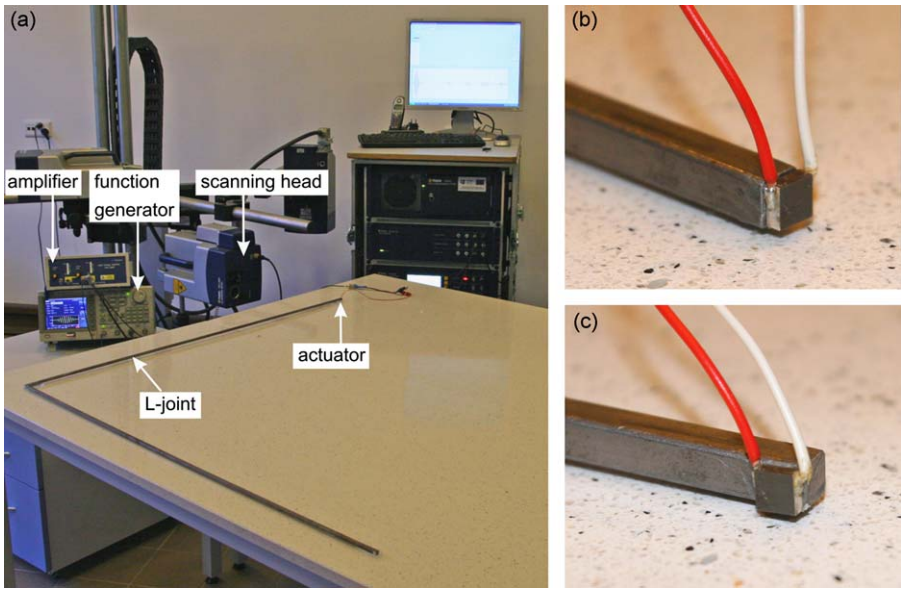

Fig. 2. Experimental setup for wave propagation: (a) hardware and L-joint specimen; (b) detail showing actuator in the case of axial wave propagation; (c) detail showing actuator in the case of flexural wave propagation.

4. Simple tests of wave propagation in a straight rod

The aim of these simple tests was to experimentally validate the numerical model of wave propagation, applied later for the L-type structure. Both longitudinal and flexural waves are considered. The placement of actuators and measurement points are shown in Fig. 3. In the considered frequency range (100–120 kHz) only one longitudinal mode and one flexural mode can propagate (Fig. 4). Modelling of longitudinal wave propagation was conducted by the spectral element method based on the Mindlin–Herrmann rod theory, whereas modelling of flexural waves was conducted by the SEM based on the Timoshenko beam theory. The choice of the Timoshenko model, even for such slender rod, is justified by particularly high excitation frequencies applied in the study. Within the frequency range of interest (100–120 kHz) the group velocity obtained by the Euler–Bernoulli beam theory differs considerably from the group velocity obtained by the Timoshenko beam theory. Additionally, the Euler–Bernoulli theory does not show the presence of the second mode (Fig. 4). Similarly, the application of the Mindlin–Herrmann rod model makes it possible to obtain more precise values of the group velocities of a wave and to obtain the second mode above the cut-off frequency (Fig. 4).

The damping matrix was assumed as proportional with respect to the mass matrix $\mathbf{C}^{(e)} = \eta \mathbf{M}^{(e)}$, with the damping parameter η set at 1000 1/s for longitudinal waves and 2000 1/s for flexural waves. The proportional damping was assumed after Ref. [24]. As it is suggested in Ref. [24], values of damping parameters were adopted to obtain the same relationship between amplitudes of reflected signals for experimental investigations and numerical simulations. The amplitude of the external force equals 1 N. In the case of flexural waves, a wave was impacted in 3rd node from the left edge, what coincides with the actuator centre. The intact specimen was modelled using 24 equal elements with 15 GLL nodes, while the specimen with the notch was modelled using 24 equal elements with 15 GLL nodes and one element with 15 GLL nodes of length 2 mm with height reduced by 1 mm. The *h*- and *p*-convergence analysis of results was carried out and elements with 15 GLL nodes were chosen as a compromise between the spectral accuracy and the relatively large time step. For the Mindlin–Herrmann as well as the Timoshenko theories, the mass matrix has the diagonal structure, therefore the temporal integration using the central difference scheme can be efficiently conducted. The time step Δt must be smaller than a critical value $\Delta t_{cr} = 2/\omega_n$, where the ω_n is the largest frequency of an assembled finite element mesh with n degrees of freedom. The time step was chosen as $\Delta t = 10^{-7}$ s for the intact specimen and $\Delta t = 10^{-8}$ s for the specimen with the notch. This is so because for the specimen with defect the largest frequency of an assembled finite element mesh is about ten times larger than for the intact specimen. In performed numerical simulations, time of temporal integration was about 8 times smaller for the Gauss-Lobatto-Legendre quadrature (which leads to the diagonal mass matrix) than for the Gauss quadrature.

Fig. 3. Location of actuator and velocity measurement points in the rod: (a) for longitudinal wave propagation; (b) for flexural wave propagation.

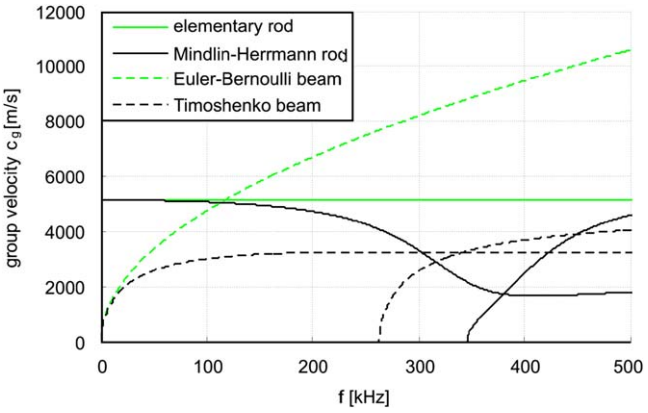

Fig. 4. Group velocity dispersion curves in the steel rod of cross-section 6 mm × 6 mm for the elementary rod, Mindlin–Herrmann rod, Euler–Bernoulli beam and Timoshenko beam theories.

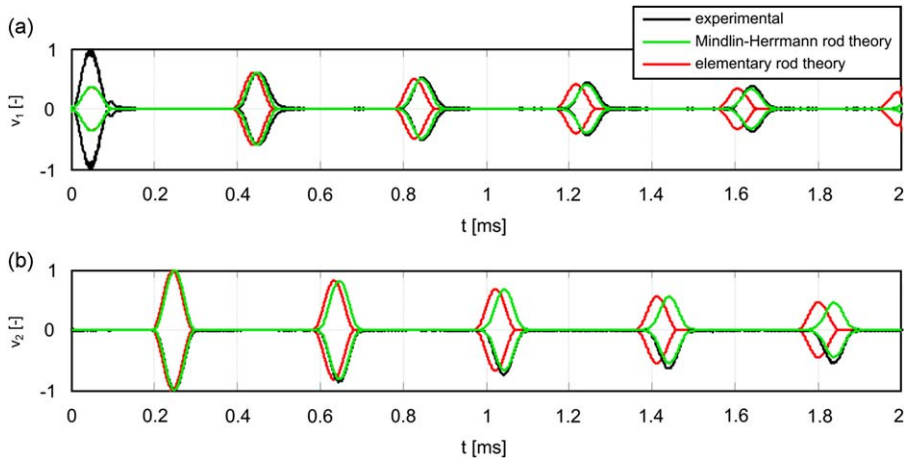

Fig. 5. Comparison between experimental and numerical velocity signals for the ideal rod in the case of longitudinal wave propagation: (a) velocity signal $v_1(t)$ registered on the left end of the rod; (b) velocity signal $v_2(t)$ registered on the right end of the rod.

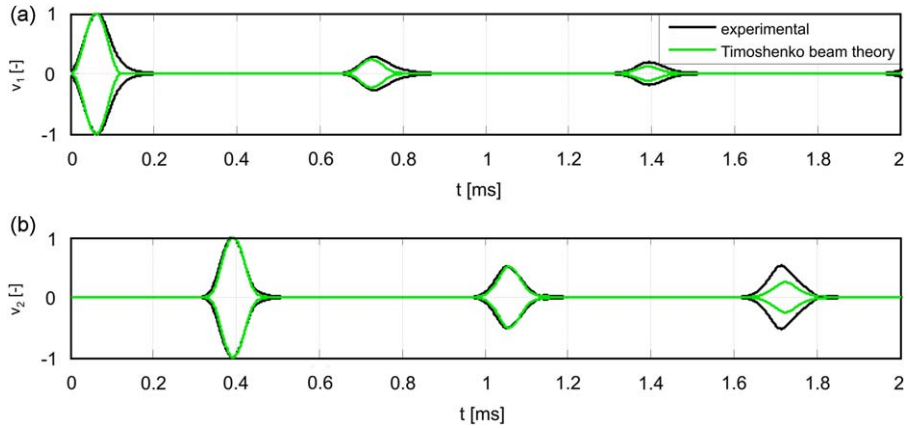

Fig. 6. Comparison between experimental and numerical velocity signals for the ideal rod in the case of flexural wave propagation: (a) velocity signal $v_1(t)$ registered on the left end of the rod; (b) velocity signal $v_2(t)$ registered on the right end of the rod.

In Fig. 5 numerical results for longitudinal wave propagation in the ideal rod are compared with experimental data for the elementary rod and Mindlin–Herrmann rod theories. Only signal envelopes are plotted for clarity. The velocity signal $v_1(t)$ was measured on the left end of the rod (Fig. 5a), while the signal $v_2(t)$ was measured on its right end (Fig. 5b). Amplitudes of experimental and numerical signals measured on the right end of the rod were normalized to 1. In the case of experimental signal measured on the left end of the rod, the normalization was carried out to the first reflection, because the signal $v_1(t)$ was measured on the actuator, not directly on the specimen. Therefore a discrepancy between amplitudes of the first pulse appears in Fig. 5a. If the elementary rod theory is used, experimental data are not compatible with numerical ones. Experimental velocity signals are delayed with respect to numerical ones. This indicates the presence of dispersion. Considering the Mindlin–Herrmann rod theory, it is noted that numerical simulations are in good agreement with experimental data. In Fig. 6 numerical results for the flexural wave propagation are compared with experimental data. It can be observed, that experimental signals are in good agreement with numerical simulations based on the Timoshenko beam theory.

The comparison of experimental velocity signals for the intact specimen with the specimen with the notch is given in Figs. 7 and 8 for longitudinal and flexural waves, respectively. For specimens with the notch, additional reflections appear in the response signal and the position of damage in the rod can easily be identified from both $v_1(t)$ and $v_2(t)$ velocity signals. However, the situation is different when damage does not occur in the middle of the rod. In the example with longitudinal wave propagation, two positions of damage, namely $L_r = 0.25L$ and $L_r = 0.75L$ were considered (Fig. 9). It can be seen, that only signal $v_1(t)$, registered at the same point as the actuator, makes an unambiguous localization of damage possible (Fig. 9a, b). The velocity signal $v_2(t)$ registered at the opposite end is the same for both $L_r = 0.25L$ and $L_r = 0.75L$ damage positions (Fig. 9c).

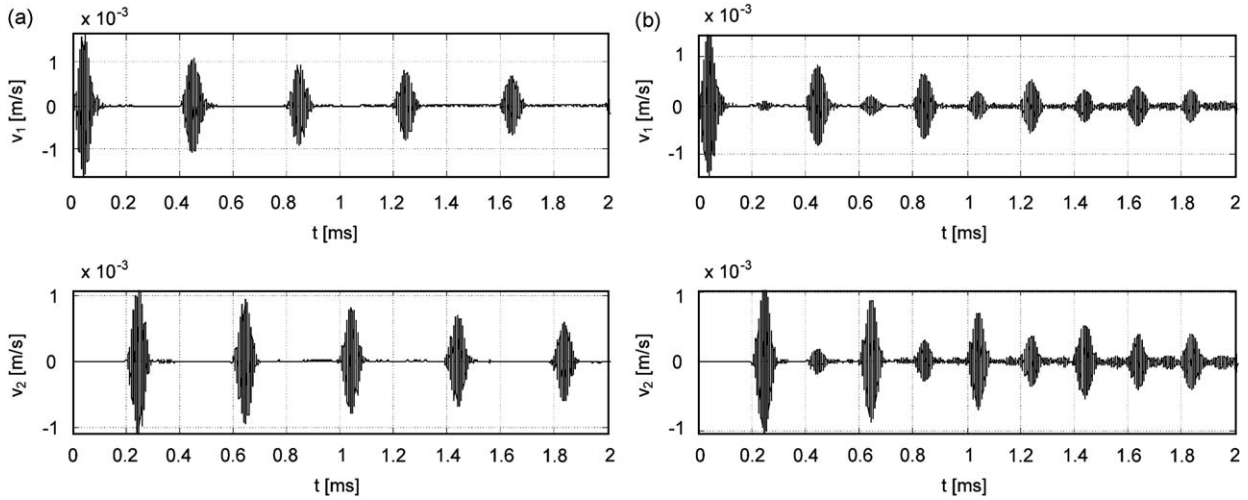

Fig. 7. Experimental velocity signals $v_1(t)$ and $v_2(t)$ measured on both ends of the rod in the case of longitudinal wave propagation: (a) ideal rod; (b) rod with the notch.

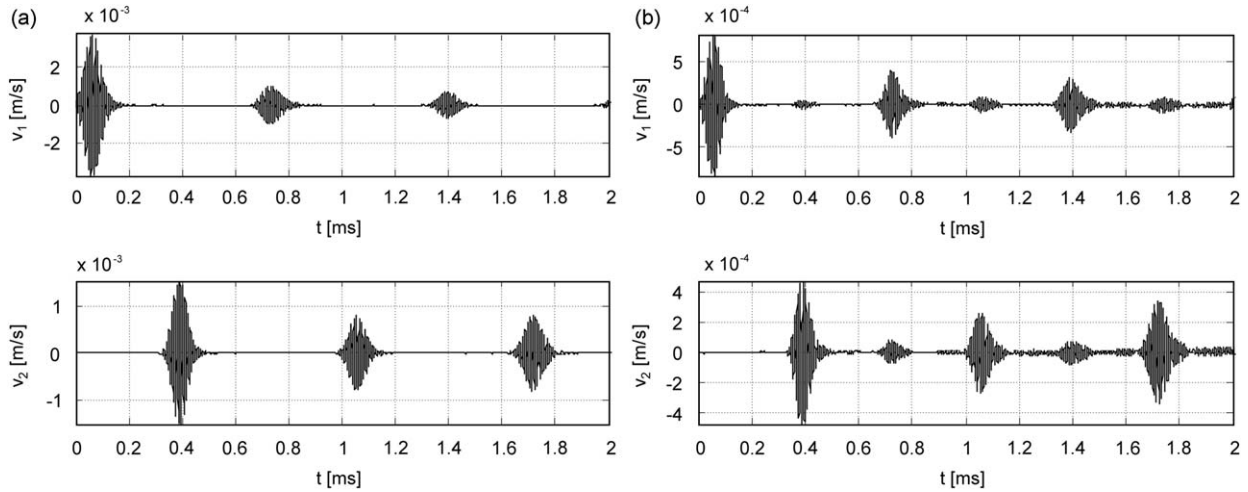

Fig. 8. Experimental velocity signals $v_1(t)$ and $v_2(t)$ measured on both ends of the rod in the case of flexural wave propagation: (a) ideal rod; (b) rod with the notch.

5. Damage detection in the L-joint by guided waves

Experimental and numerical investigations were performed for the ideal L-joint as well as for the L-joint with the notch (Fig. 1c, d). Two positions of the notch were considered, namely the notch on the horizontal member and on the vertical member. A load in the form of a wave packet was induced in both axial and transverse directions. In numerical simulations the *M-H-Tim* spectral frame element was applied. The L-type joints were modelled by the SEM in the same way as the simple rods (as described in Section 4). The first non-zero frequency is 23.41 Hz for the intact L-joint and 23.39 Hz for the L-joint with the notch. For the applied mesh the highest frequencies, which affect the critical time step Δt_{cr} are 2.93 MHz for the intact L-joint and 30.62 MHz for the L-joint with the notch.

5.1. Spectral element method model of the L-joint

The L-joint contains the butt weld in the corner. In this paper, it is proposed to model the welded part of a rod as a part with reduced modulus of elasticity. To justify this assumption, a simple wave propagation test on a straight rod containing a butt weld of length 4 mm was performed (Fig. 10a). The rod was cut in two parts, the edges of both pieces were chamfered doubly in two directions (Fig. 10b) and the welding was performed. Then the weld was grinded in such a way,

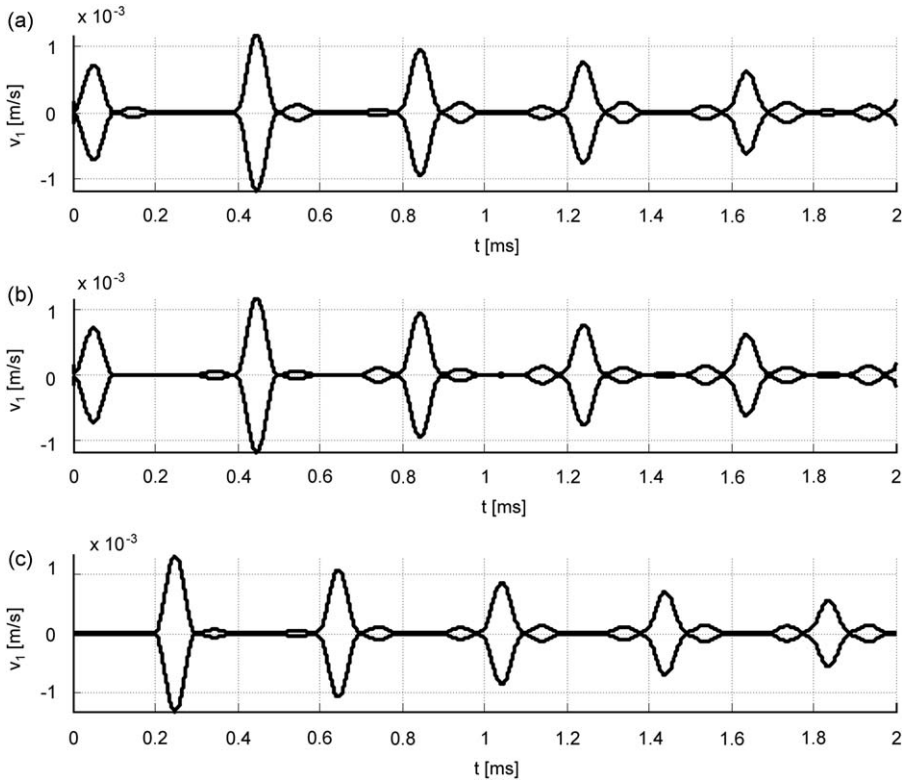

Fig. 9. Envelopes of numerical velocity signals $v_1(t)$ and $v_2(t)$ measured on both ends of the rod containing the notch at position L_r in the case of longitudinal wave propagation: (a) notch at $L_r = 0.25L$; (b) notch at $L_r = 0.75L$; (c) notch at $L_r = 0.25L$ or $L_r = 0.75L$.

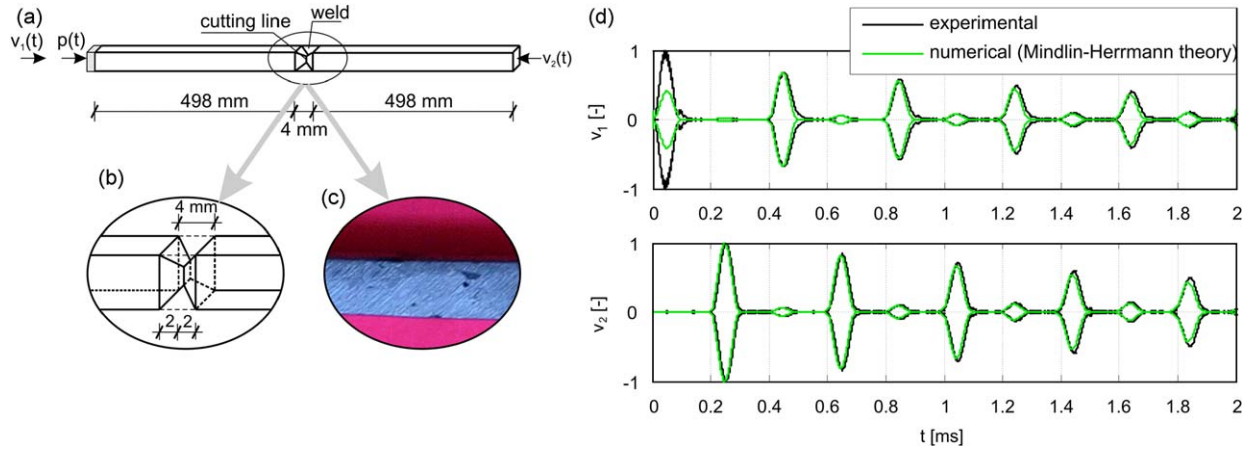

Fig. 10. Straight rod with the weld analyzed to validate numerical weld model: (a) geometry; (b) detail of the weld; (c) the photo of the place of the weld; (d) comparison between experimental and numerical velocity signals in the case of longitudinal wave propagation.

that the rod obtained its origin cross-section (Fig. 10c). In numerical simulations, it was assumed, that the part of the rod with the weld has degradated parameters because of heating during the welding process. After extended numerical investigations, a 10 percent level of reduction of the material modulus of elasticity was chosen. This was confirmed by experimental analysis. Therefore the SEM model of the rod has 4 mm element in the middle of the rod having the modulus of elasticity E=180.10 GPa, i.e. 10 percent reduced compare with the remaining part of the rod. The measured velocity signals $v_1(t)$ and $v_2(t)$ were compared with the numerical ones and displayed in Fig. 10d. It can be noted that the experimental results agree with the numerical ones. The proposed weld model provided velocity results compatible with experimentally measured signals.

In the next step, the numerical model of the L-joint with the weld was prepared. Following the experiment with the straight rod, it was assumed that two elements near the corner are with 10 percent reduced modulus of elasticity compare with the remaining part of the L-joint. The length of each element was established as 2 cm, because the influence of the welding process was observed on this length. Additionally, the numerical analysis of the isotropic L-joint was performed. Fig. 11 shows comparison of the velocity signal $v_1(t)$ registered in the node 1 (Fig. 12a) for the isotropic L-joint and for the L-joint with the weld. Both spectral models (for the isotropic L-joint and for the L-joint with the weld) provide the same results. This is because, the propagating waves reflect from the corner, and the reflection from the weld is masked by the reflection from the L-joint corner. Therefore, in further simulations, the SEM model of the L-joint was assumed to be isotropic, despite of the presence of the weld in its corner.

5.2. Longitudinal wave propagation in the L-joint

The wave packet of frequency 120 kHz was imposed in the longitudinal direction at the node 1, whereas the velocity was measured in both nodes 1 and 2 (Fig. 12). At first the ideal frame was examined (Fig. 12a). Experimental and numerical signals for this case are illustrated in Fig. 13. When the incident longitudinal wave reached the frame corner (node 3), both longitudinal and flexural waves propagated and reflected. In the $v_1(t)$ signal (Fig. 13a), the incident wave and eight reflections are visible within the recorded 2 ms time period. The 1st, 2nd, 4th and 6th reflections were caused by propagation of the longitudinal wave only, whereas the 3rd, 5th, 7th and 8th reflections contains both longitudinal and flexural components. Similarly, in the $v_2(t)$ velocity signal (Fig. 13b), the 1st, 2nd, 4th and 6th waveforms were created by propagation of longitudinal waves, while the 3rd, 5th, 7th and 8th waveforms appeared from both longitudinal and flexural waves. In Fig. 13 experimental and numerical signals in form of signal envelopes are shown and compared for the ideal L-joint. It can be seen, that the application of the numerical model based on the *M-H-Tim* spectral frame element provides experimental data compatible with numerical ones with respect to times of reflections.

The second example concerns the L-joint with the notch on the horizontal member (Fig. 12b). Numerical and experimental results for this case are compared in Fig. 14. Reflections from the notch are visible in both $v_1(t)$ and $v_2(t)$ numerical signals. Reflections from damage were identified based on the knowledge of the L-joint geometry and the group

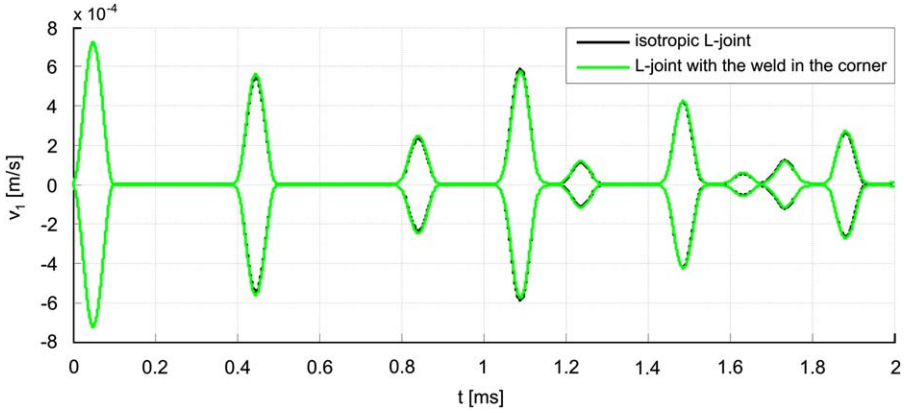

Fig. 11. Numerical velocity signals for the isotropic L-joint and L-joint with the weld.

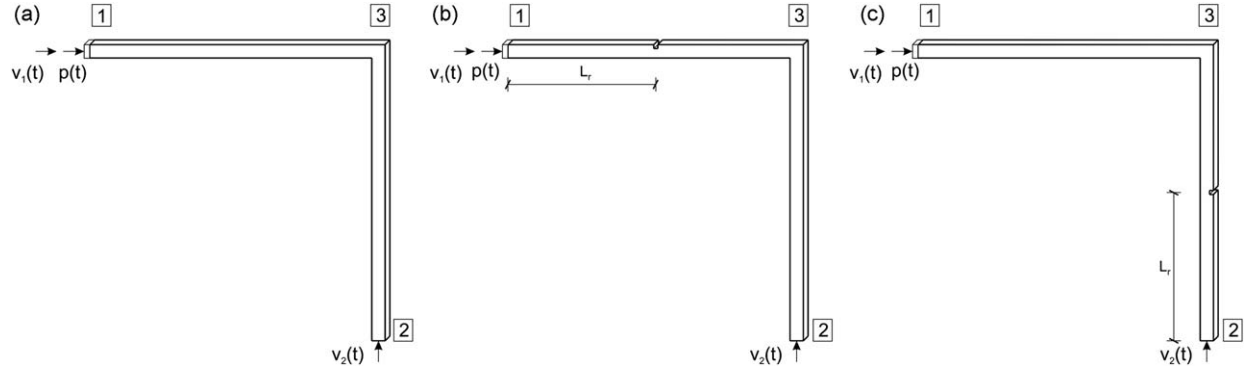

Fig. 12. Location of actuators and velocity measurements points for the L-joint in the case of longitudinal wave propagation: (a) ideal L-joint; (b) L-joint with the notch at the horizontal member; (c) L-joint with the notch at the vertical member.

velocity of axial and flexural waves. Two distinct reflections from the notch appeared in the $v_1(t)$ signal (Fig. 14a), namely at the time instant equal to 0.2 and 0.6 ms. These both reflections were caused by propagation of longitudinal waves. In the $v_2(t)$ signal (Fig. 14b) two reflections from the notch can also be observed. The first reflection occurred in 0.6 ms as a result of propagation of the longitudinal wave. The second reflection was caused by propagation of both longitudinal and flexural waves and it occurred at the time instance equal to 0.73 ms (the longitudinal wave from the node 1 to the node 3, next the flexural wave from the node 3 to the notch and back, finally the longitudinal wave from the node 3 to the node 2). Next reflections from the notch overlaped with reflections from the L-joint corner and from the L-joint ends, therefore they cannot be easily identified. In experimentally measured signals, reflections from the notch can also be observed in Fig. 14. Reflections contained in the $v_1(t)$ signal are very distinct; however reflections from the notch in the $v_2(t)$ experimental signal are more contaminated.

In the third example, the notch on the vertical member of the L-joint is considered (Fig. 12c) and results for this case are presented in Fig. 15. In the $v_1(t)$ numerical signal (Fig. 15a) the reflection from the notch caused by longitudinal wave

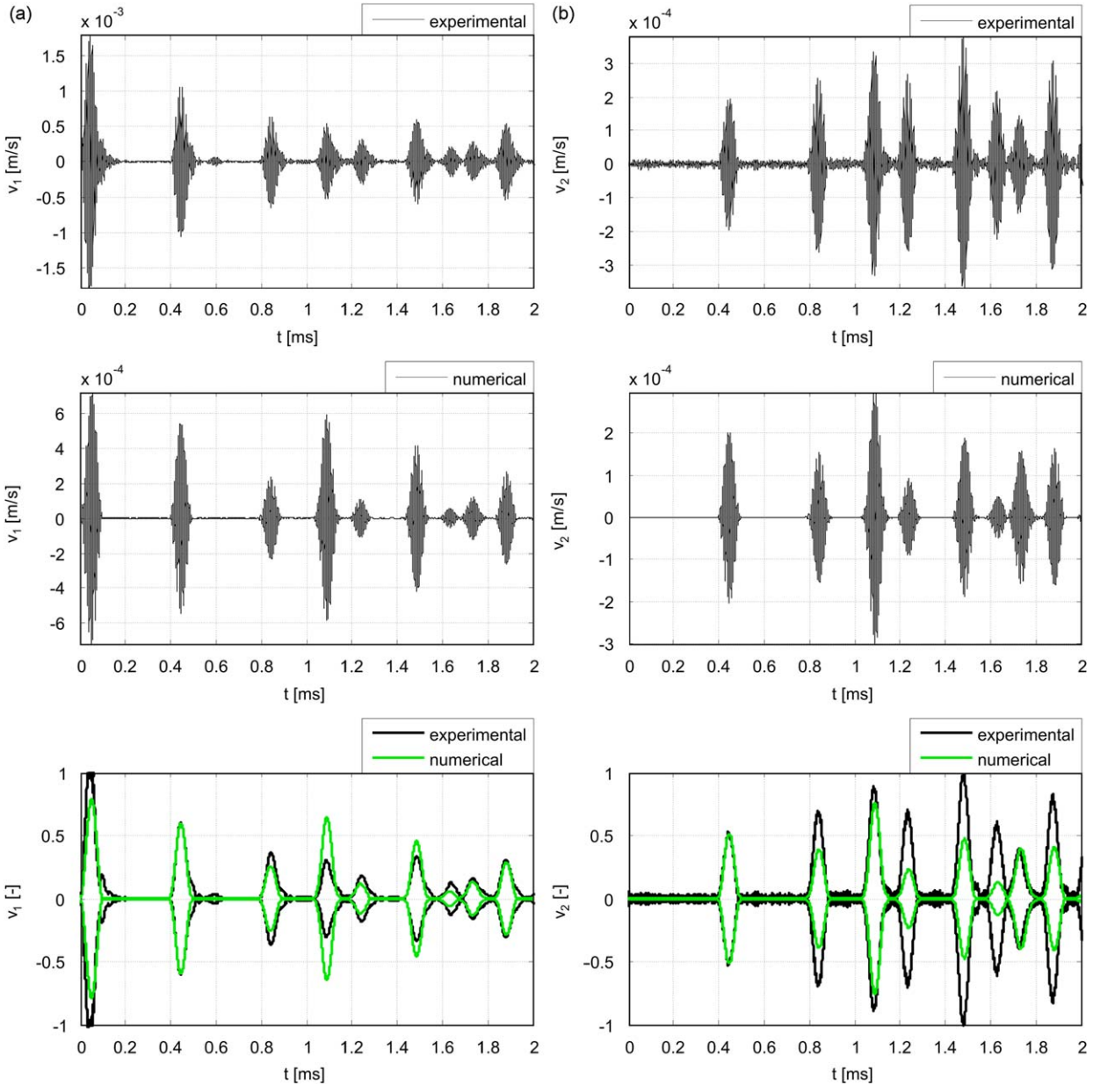

Fig. 13. Comparison between experimental and numerical velocity time signals for the ideal L-joint in the case of longitudinal wave propagation: (a) velocity signal $v_1(t)$ registered on the left end of the L-joint; (b) velocity signal $v_2(t)$ registered on the right end of the L-joint.

propagation occurring in the time instance t=0.6 ms have very small amplitude and its usefulness in damage detection is limited because the experimental measurement of such small waveform appeared to be impossible. The second reflection from the notch in the $v_1(t)$ occurred at 0.73 ms and it was caused by propagation of longitudinal and flexural waves (the longitudinal wave from the node 1 to the corner, than flexural to the notch and back, and finally the longitudinal wave from the corner to the node 1). This component can be used for damage detection purpose and it was successfully recorded in the performed experiment. The numerical velocity signal $v_2(t)$ (Fig. 15b) is identical as in the case of the notch on the horizontal element. Hence it is impossible to indicate the precise localization of damage (i.e. if it is on the vertical or on the horizontal element) based on the information from the $v_2(t)$ only for considered position of damage.

The last example concerns the numerical simulations for various damage positions L_r, namely $L_r = 0.25L$, $L_r = 0.5L$ and $L_r = 0.75L$ (cf. Fig. 12b and c). As in the case of the simple rod, the measurement of the velocity signal $v_2(t)$ cannot provide unambiguous identification of damage position. If damage is situated on the horizontal member of the L-joint (i.e. on the

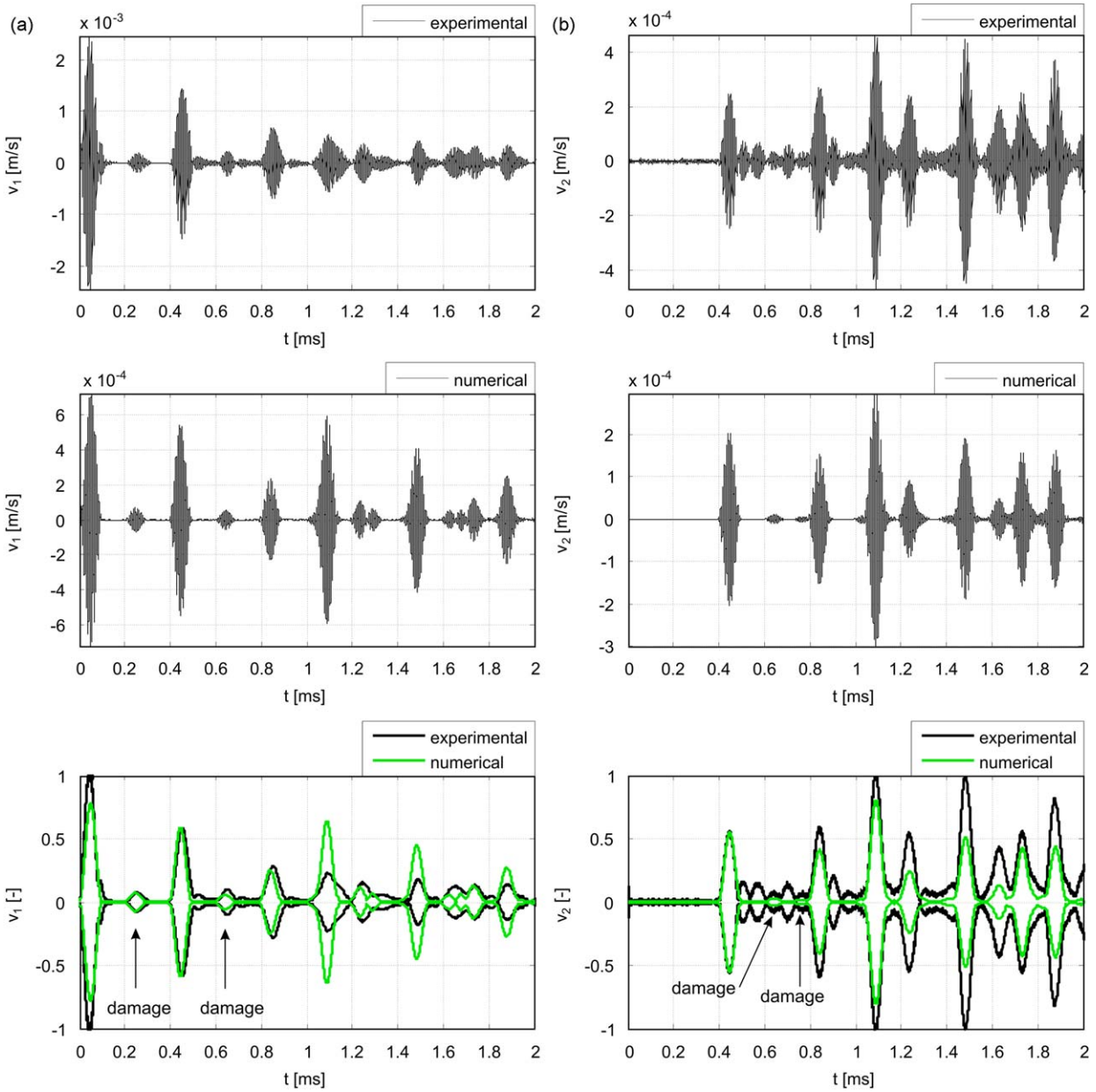

Fig. 14. Comparison between experimental and numerical velocity time signals for the L-joint with the notch at the horizontal member in the case of longitudinal wave propagation: (a) velocity signal $v_1(t)$ registered on the left end of the L-joint; (b) velocity signal $v_2(t)$ registered on the right end of the L-joint.

member, on which the actuator is bonded), the velocity signal $v_1(t)$ enables easy localization of the notch position (Fig. 16a). However, when damage is placed on the vertical member, the reflection from damage is masked partially by the reflection from the node 2. As shown in Fig. 16b, the localization of the notch is possible for all considered positions ($L_r = 0.25L$, $L_r = 0.5L$, $L_r = 0.75L$), however damage placed in the neighbourhood of $L_r = 0.6L$ to $L_r = 0.7L$ will be completely masked by the reflection from the node 2. This is caused by different values of group velocities of the longitudinal wave (5039 m/s) and the flexural wave (3021 m/s). If the group velocity of the longitudinal wave was equalled to the group velocity of the flexural wave (here for the frequency 303 kHz), this ambiguous situation could be eliminated. However, for the equal group velocities of the longitudinal and flexural waves, the second flexural mode appears which makes the damage detection more difficult.

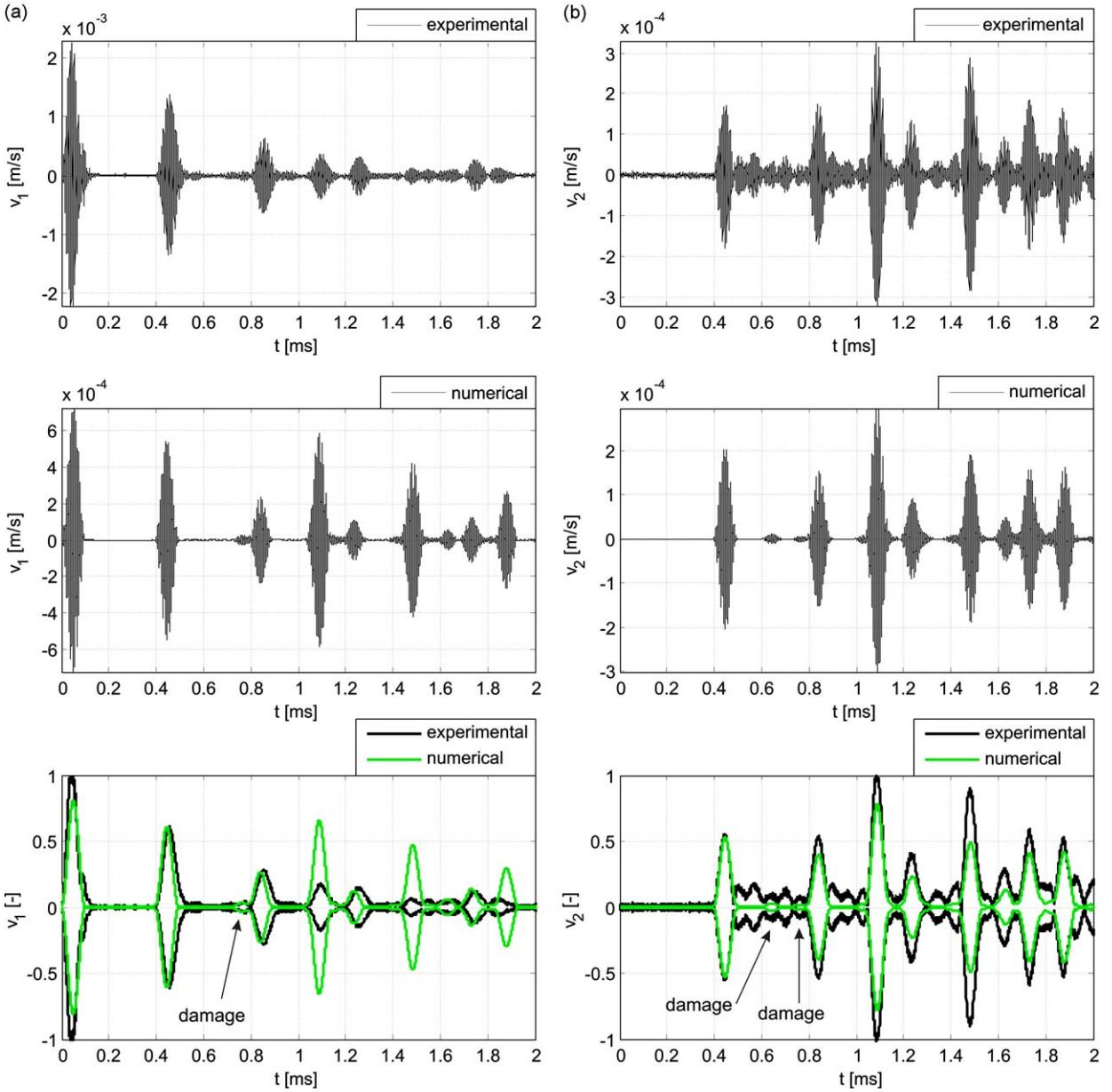

Fig. 15. Comparison between experimental and numerical velocity time signals for the L-joint with the notch at the vertical member in the case of longitudinal wave propagation: (a) velocity signal $v_1(t)$ registered on the left end of the L-joint; (b) velocity signal $v_2(t)$ registered on the right end of the L-joint.

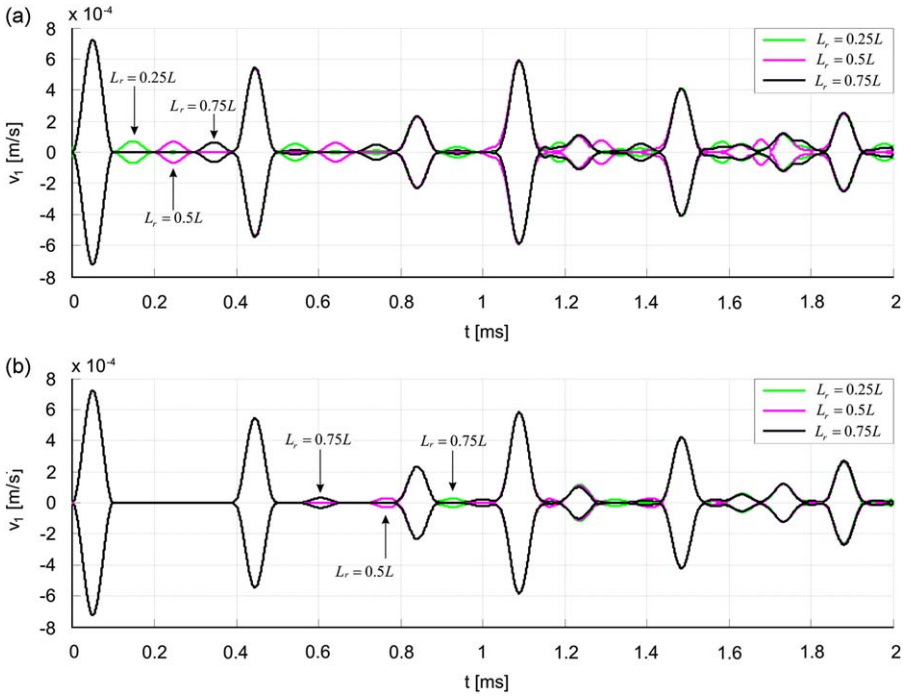

Fig. 16. Envelopes of numerical velocity signals $v_1(t)$ measured on the left end of the L-joint containing the notch for different positions L_r ($L_r = 0.25L$, $L_r = 0.5L$, $L_r = 0.75L$) in the case of longitudinal wave propagation: (a) L-joint with the notch at the horizontal member; (b) L-joint with the notch at the vertical member.

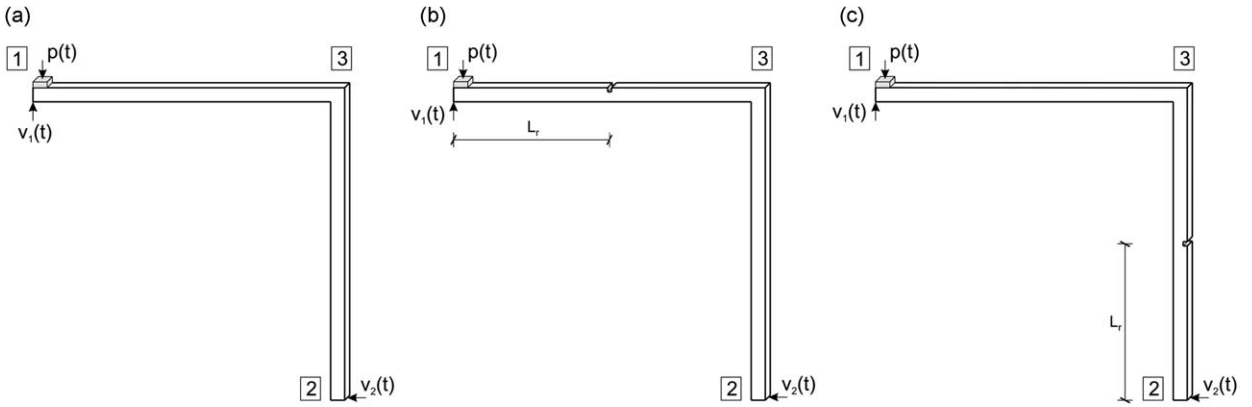

Fig. 17. Location of actuators and velocity measurements points for the L-joint in the case of flexural wave propagation: (a) ideal L-joint; (b) L-joint with the notch at the horizontal member; (c) L-joint with the notch at the vertical member.

5.3. *Flexural wave propagation in the L-joint*

The incident wave packet of frequency 100 kHz was imposed in the transverse direction, while the velocity was measured in both nodes 1 and 2, as it is shown in Fig. 17. At the beginning, the ideal L-joint was investigated (Fig. 17a). When the incident flexural wave reached the frame corner, both flexural and longitudinal waves appeared. The group velocity of the axial wave is equal to 5075 m/s, while the group velocity of the flexural wave is 2950 m/s. Results of numerical simulations and experiments are given in Fig. 18. In the $v_1(t)$ signal (Fig. 18a), the incident wave and six echoes were visible during recorded 2 ms time period. The 1st and 3rd reflections were caused by propagation of the flexural wave, whereas the 2nd, 4th, 5th and 6th reflections contained both flexural and longitudinal components. The comparison of numerical and experimental signals in the form of signal envelopes for the ideal L-joint is illustrated in Fig. 18. Note that the application of the numerical model based on the *M-H-Tim* spectral frame element results in compatibility of time of reflections.

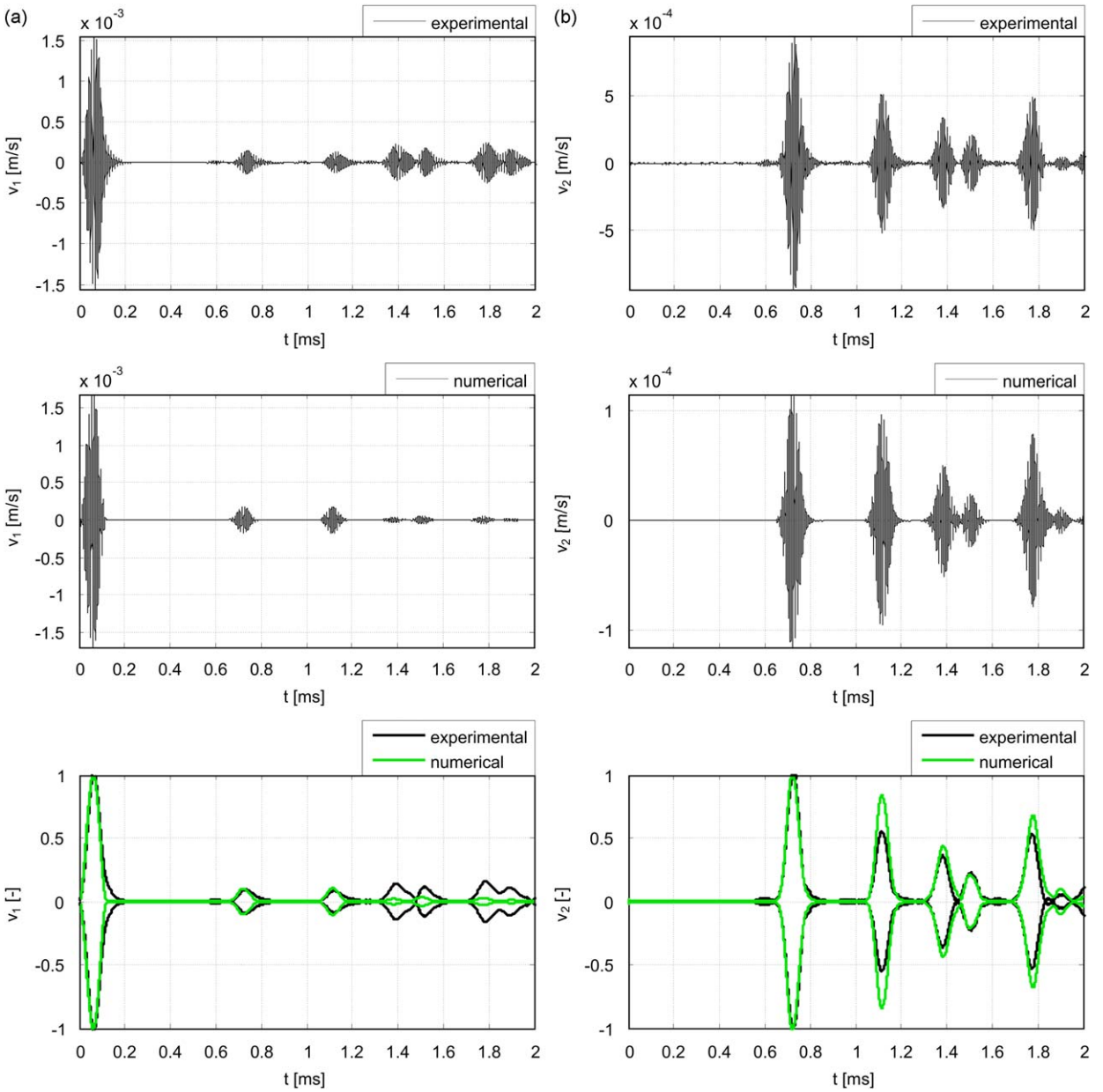

Fig. 18. Comparison between experimental and numerical velocity time signals for the ideal L-joint in the case of flexural wave propagation: (a) velocity signal $v_1(t)$ registered on the left end of the L-joint; (b) velocity signal $v_2(t)$ registered on the right end of the L-joint.

Next, the L-joint with the notch was tested. The numerically obtained $v_2(t)$ velocity signal for the L-joint with the notch on the horizontal member (Fig. 19b) is identical as for the L-joint with the notch on the vertical member (Fig. 20b). The reflection from damage occurred at 0.86 ms. Experimental signals $v_2(t)$ are also very similar for the notch situated on the horizontal and the vertical member. The signal $v_1(t)$ differs depending on the notch position (on the horizontal or on the vertical member). In the case of damage placed on the horizontal member, the reflection occurs at 0.33 ms, what was successfully registered in experimental measurements (Fig. 19a). For damage situated on the vertical element, the $v_1(t)$ signal (Fig. 20a) contained the reflection from damage at 0.86 ms (the flexural wave from the node 1 to the corner, then the longitudinal wave to the notch and back, and finally flexural wave to the node 1).

In the last example, numerical simulations for three various damage positions $L_r = 0.25L$, $L_r = 0.5L$ and $L_r = 0.75L$ are investigated (cf. Fig. 17b and c). Damage situated on the horizontal member can easily be identified from the $v_1(t)$ signal (Fig. 21a) by propagation of the flexural wave. For the notch situated on the vertical element, identification is also unambiguous for arbitrary damage position (Fig. 21b) until the group velocity of the longitudinal wave is larger than the group velocity of the flexural wave.

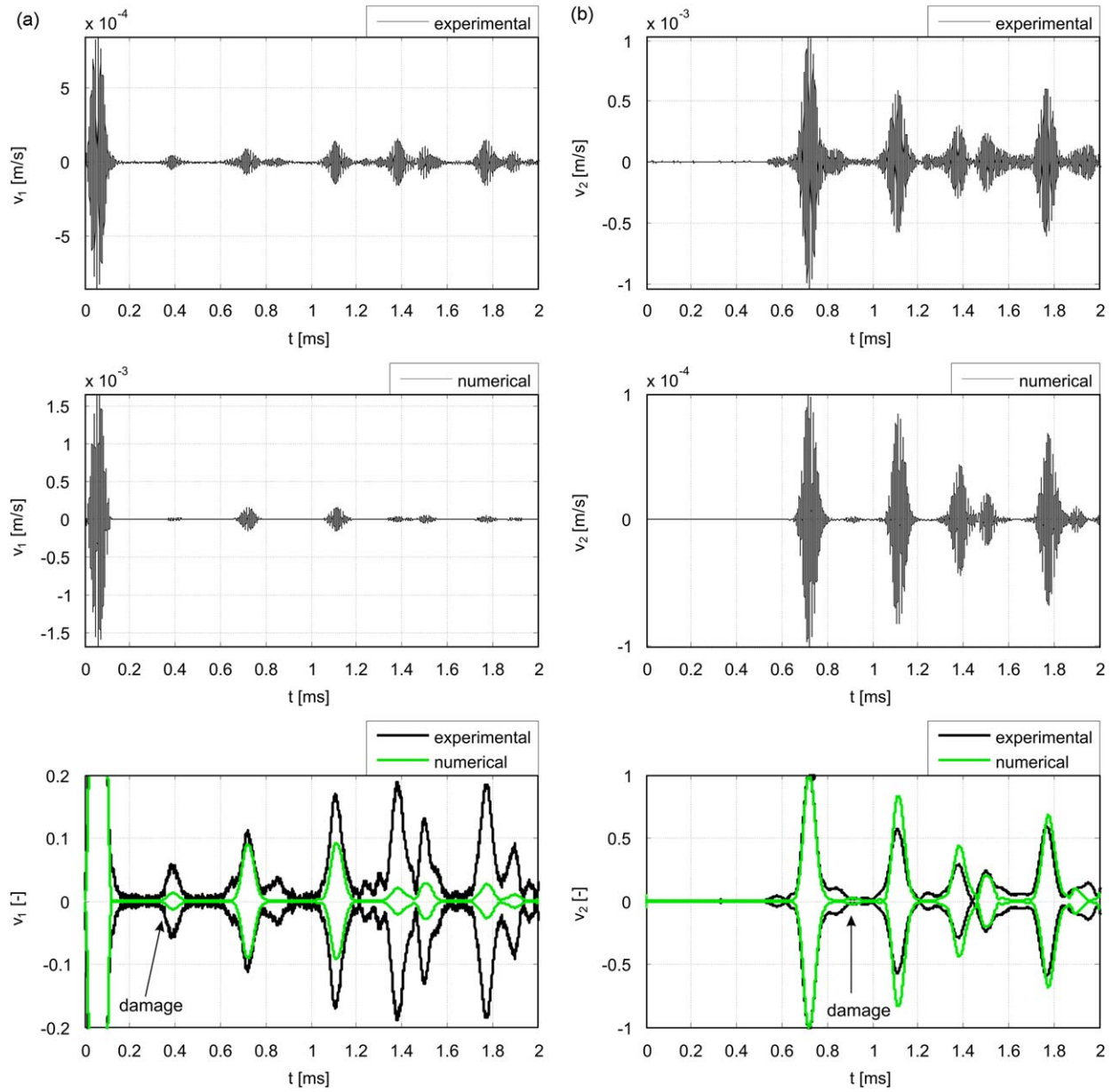

Fig. 19. Comparison between experimental and numerical velocity time signals for the L-joint with the notch at the horizontal member in the case of flexural wave propagation: (a) velocity signal $v_1(t)$ registered on the left end of the L-joint; (b) velocity signal $v_2(t)$ registered on right the end of the L-joint.

6. Conclusions

In this paper longitudinal and flexural wave propagation in the L-type joint was investigated both experimentally and numerically. In particular the detection of damage was considered by analyzing wave speeds and reflection times in recorded velocity signals.

Numerical simulations were performed by the spectral element method in the time domain using the *M-H-Tim* frame element based on the Mindlin–Herrmann rod combined with the Timoshenko beam. Application of the *M-H-Tim* element guarantees that the mass matrix has diagonal structure; therefore the temporal integration can be efficiently performed by the central difference scheme. The effectiveness of the proposed element was experimentally confirmed. The model based on the Mindlin–Herrmann rod theory guarantees better approximation for the first longitudinal mode behaviour than the elementary theory, what was proved by the comparison with experimentally measured signals. Therefore, a numerical

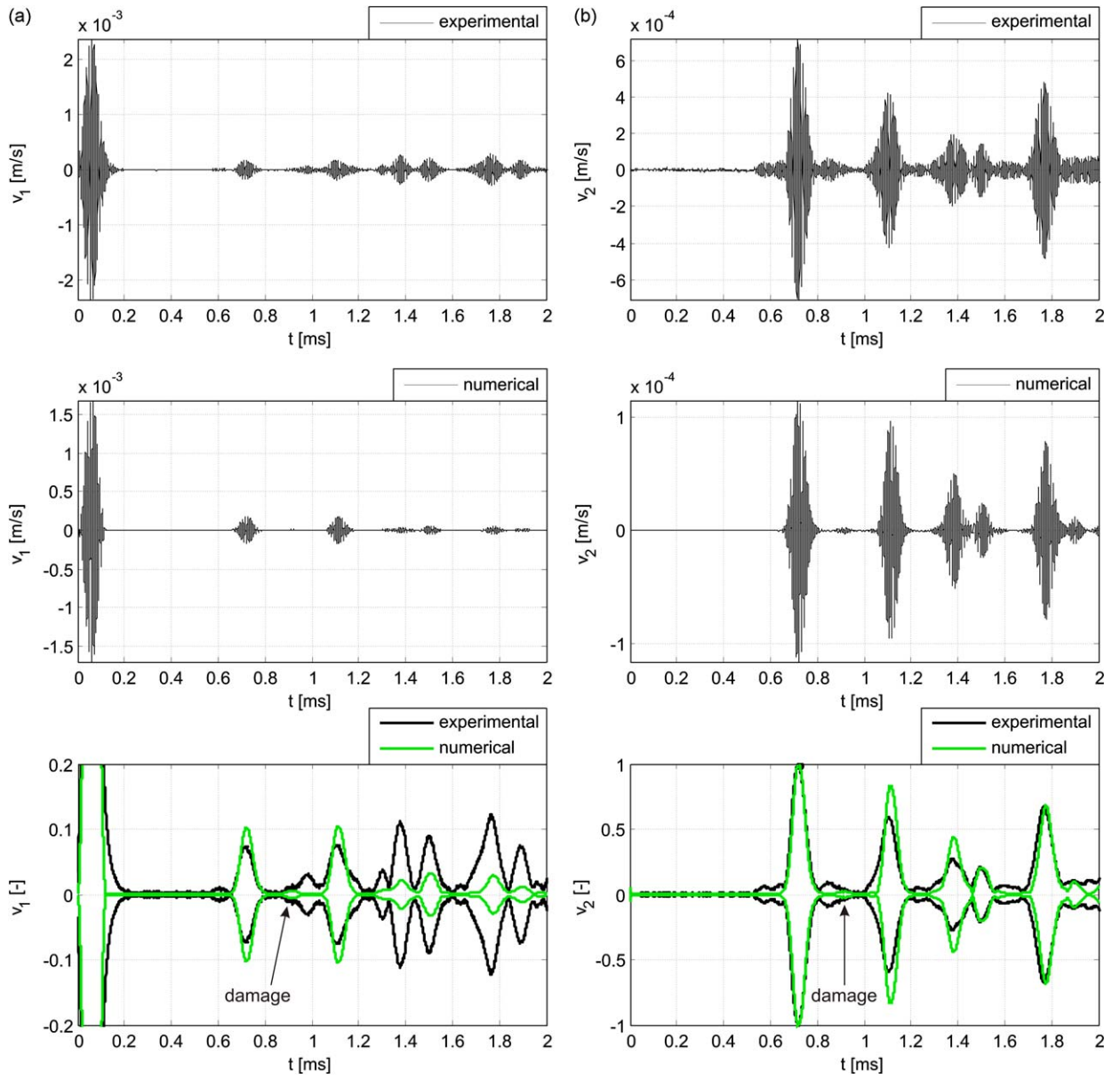

Fig. 20. Comparison between experimental and numerical velocity time signals for the L-joint with the notch at the vertical member in the case of flexural wave propagation: (a) velocity signal $v_1(t)$ registered on the left end of the L-joint; (b) velocity signal $v_2(t)$ registered on the right end of the L-joint.

model of an arbitrary joint intended as a part of the SHM system should be described in the SEM formulation based on the Mindlin–Herrmann and the Timoshenko theories to obtain proper times of reflections from potential damage.

Experimental and numerical investigations of damage detection were performed for the L-joint with a reference to the simple rod. In the performed experiments, the velocity signal was measured at two opposite ends of the specimen (at the 'start point', on which the actuator is bonded and at the 'end point'). The frequency of the applied incident wave was selected to ensure propagation one axial and one flexural mode. Damage detection in the rod is possible using longitudinal as well as flexural waves and it is unambiguous, when the velocity signal is measured at the start point. Localization of damage in the L-joint is more difficult to detect due to the mode conversion. As in the case of the simple rod, the measurement of the wave propagation signal at the end point cannot provide unambiguous identification of damage position. For longitudinal as well as for flexural incident waves, damage situated on the horizontal member (containing the excitation point) can easily be identified by the velocity measurement in the start point. When damage is situated on the vertical element (after passing of the wave through the corner), the signal registered in the start point not always can

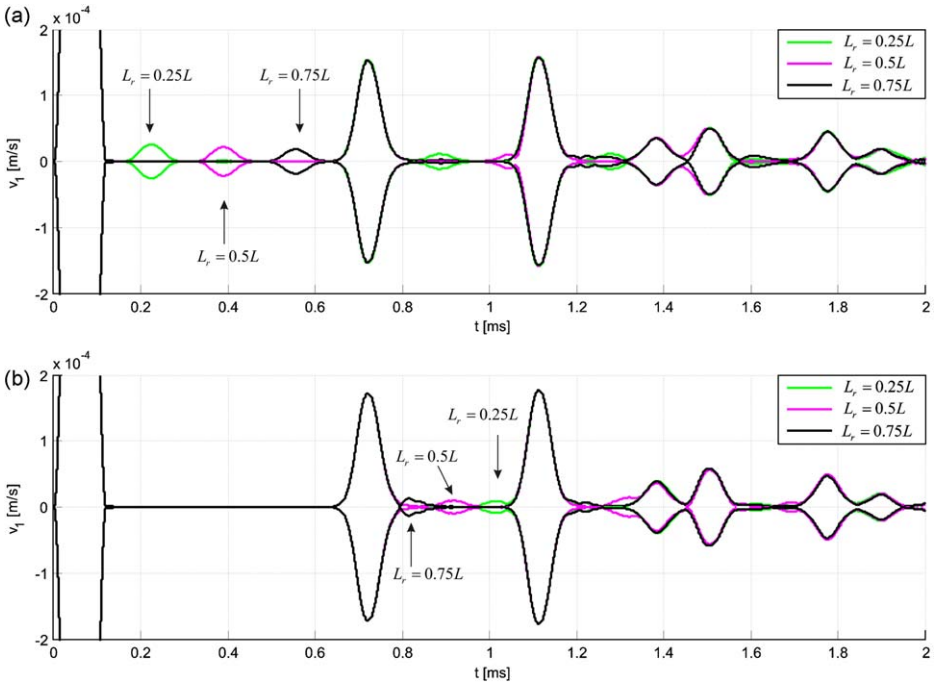

Fig. 21. Envelopes of numerical velocity signals $v_1(t)$ measured on the left end of the L-joint containing the notch for different positions L_r ($L_r = 0.25L$, $L_r = 0.5L$, $L_r = 0.75L$) in the case of flexural wave propagation: (a) L-joint with the notch at the horizontal member; (b) L-joint with the notch at the vertical member.

provide its precise localization. For the longitudinal incident wave, there is a region, in which reflection originating from damage is masked by the reflection from the L-joint ends. The location of this region depends on group velocities of axial and flexural waves. In the case of the flexural incident wave, identification of the notch is unambiguous for arbitrary damage position until the group velocity of the longitudinal wave is larger than the group velocity of the flexural wave. Results of the research on the effectiveness of the guided wave-base damage detection technique lead to the conclusion, that the SHM system designed for the L-joint structure can be equipped with only one actuator and one measurement point (in the same place as the actuator) since the detection of damage using the flexural incident wave is possible for an arbitrary damage position.

Acknowledgements

The author is grateful for the support of the Polish Ministry of Science and Higher Education via Grant no. N506 065 31/3149 entitled: "Multilevel damage detection system in engineering structures".

References

[1] V. Giurgiutiu, *Structural Health Monitoring with Piezoelectric Wafer Active Sensors*, Academic Press, 2008.
[2] D.E. Adams, *Health Monitoring of Structural Materials and Components. Methods with Applications*, Wiley, 2007.
[3] L. Yu, V. Giurgiutiu, In situ 2-D piezoelectric wafer active sensors array for guided wave damage detection, *Ultrasonics* 48 (2008) 117–134.
[4] P. Cawley, D. Alleyne, The use of lamb waves for the long range inspection of large structures, *Ultrasonics* 34 (1996) 287–290.
[5] M.J.S. Lowe, D.N. Alleyne, P. Cawley, Defect detection in pipes using guided waves, *Ultrasonics* 36 (1998) 147–154.
[6] J.L. Rose, M.J. Avioli, P. Mudge, R. Sanderson, Guided wave inspection potential defects in rail, *NDT&E International* 37 (2004) 153–161.
[7] C.M. Lee, J.L. Rose, Y. Cho, A guided wave approach to defect detection under shelling in rail, *NDT&E International* 42 (2009) 174–180.
[8] V. Giurgiutiu, A. Zagrai, J. Bao, Damage identification in aging aircraft structures with piezoelectric wafer active sensors, *Journal of Intelligent Material Systems and Structures* 15 (2004) 673–687.
[9] R.P. Dalton, P. Cawley, M.J.S. Lowe, The potential of guided waves for monitoring large areas of metallic aircraft fuselage structures, *Journal of Nondestructive Evaluation* 20 (2001) 29–46.
[10] J.F. Doyle, *Wave Propagation in Structures: Spectral Analysis using Fast Discrete Fourier Transforms*, second ed., Springer-Verlag, New York, 1997.
[11] S. Gopalakrishnan, A. Chakraborty, D.R. Mahapatra, *Spectral Finite Element Method: Wave Propagation, Diagnostics and Control in Anisotropic and Inhomogeneous Structures*, Springer-Verlag, London, 2008.
[12] M. Palacz, M. Krawczuk, Analysis of longitudinal wave propagation in a cracked rod by the spectral element method, *Computers & Structures* 80 (2002) 1809–1816.
[13] M. Krawczuk, M. Palacz, W. Ostachowicz, The dynamic analysis of a cracked Timoshenko beam by the spectral element method, *Journal of Sound and Vibration* 264 (2003) 1139–1153.

[14] M. Krawczuk, M. Palacz, W. Ostachowicz, Wave propagation in plate structures for crack detection, *Finite Elements in Analysis and Design* 40 (2004) 991–1004.
[15] D.R. Mahapatra, S. Gopalakrishnan, T.S. Sankar, Spectral-element-based solutions for wave propagation analysis of multiply connected unsymmetric laminated composite beams, *Journal of Sound and Vibration* 237 (2000) 819–836.
[16] M. Mitra, S. Gopalakrishnan, Extraction of wave characteristics from wavelet-based spectral finite element formulation, *Mechanical Systems and Signal Processing* 20 (2006) 2046–2079.
[17] M. Mitra, S. Gopalakrishnan, Spectrally formulated wavelet finite element for wave propagation and impact force identification in connected 1-D waveguides, *International Journal of Solids and Structures* 42 (2005) 4695–4721.
[18] H. Igawa, K. Komatsu, I. Yamaguchi, T. Kasai, Wave propagation analysis of frame structures using the spectral element method, *Journal of Sound and Vibration* 227 (2004) 1071–1081.
[19] F. Moser, L.J. Jacobs, J. Qu, Modeling elastic wave propagation in waveguides with the finite element method, *NDT&E International* 32 (1999) 225–234.
[20] S. Gopalakrishnan, A deep rod finite element for structural dynamics and wave propagation problems, *International Journal for Numerical Methods in Engineering* 48 (2000) 731–744.
[21] T. Patera, A spectral element method for fluid dynamics: laminar flow in a channel expansion, *Journal of Computational Physics* 54 (1984) 468–488.
[22] C. Canuto, M.Y. Hussaini, A. Quarteroni, T.A. Zang, *Spectral Methods in Fluid Dynamics*, Springer-Verlag, Berlin Heidelberg, 1998.
[23] R. Sridhar, A. Chakraborty, S. Gopalakrishnan, Wave propagation analysis in anisotropic and inhomogeneous uncracked and cracked structures using pseudospectral finite element method, *International Journal of Solids and Structures* 43 (2006) 4997–5031.
[24] P. Kudela, M. Krawczuk, W. Ostachowicz, Wave propagation modelling in 1D structures using spectral finite elements, *Journal of Sound and Vibration* 300 (2007) 88–100.
[25] A. Żak, M. Krawczuk, W. Ostachowicz, Propagation of in-plane wave in an isotropic panel with a crack, *Finite Elements in Analysis and Design* 42 (2006) 929–941.
[26] P. Kudela, A. Żak, M. Krawczuk, W. Ostachowicz, Modelling of wave propagation in composite plates using the time domain spectral element method, *Journal of Sound and Vibration* 302 (2007) 728–745.
[27] J. Chróścielewski, M. Rucka, K. Wilde, W. Witkowski, Formulation of spectral truss element for guided waves damage detection in spatial steel trusses, *Archives of Civil Engineering LV* (2009) 43–63.
[28] H. Peng, G. Meng, F. Li, Modeling of wave propagation in plate structures using three-dimensional spectral element method for damage detection, *Journal of Sound and Vibration* 320 (2009) 942–954.
[29] J.P. Lee, H. Kolsky, The generation of stress pulses at the junction of two non-collinear rods, *Journal of Applied Mechanics* 39 (1972) 809–813.
[30] K.J. Atkins, S.C. Hunter, The propagation of longitudinal elastic waves around right-angled corners in rods of square cross section, *The Quarterly Journal of Mechanics and Applied Mathematics* 28 (1975) 245–260.
[31] M.-T. Liang, C.-J. Chen, Investigation of longitudinal elastic wave at right-angle joint of two rods, *Journal of Marine Science and Technology* 6 (1998) 45–53.
[32] R. Beccu, C.M. Wu, B. Lundberg, Reflection and transmission of the energy of transient elastic extensional waves in a bent bar, *Journal of Sound and Vibration* 191 (1996) 261–272.
[33] J.F. Doyle, T.N. Farris, A spectrally formulated element for wave propagation in 3-D frame structures, *The International Journal of Analytical and Experimental Modal Analysis* 5 (1990) 223–227.
[34] M. Martin, S. Gopalakrishnan, J.F. Doyle, Wave propagation in multiply connected deep waveguides, *Journal of Sound and Vibration* 174 (1994) 521–538.
[35] R.D. Mindlin, G. Herrmann, A one dimensional theory of compressional waves in an elastic rod, *Proceedings of First US National Congress of Applied Mechanics*, 1950, pp. 187–191.
[36] T.J.R. Hughes, *The Finite Element Method: Linear Static and Dynamics Finite Element Analysis*, Dover Publications, Inc., Mineola, New York, 2000.
[37] K.J. Bathe, *Finite Element Procedures*, Prentice Hall, Upper Saddle River, 1996.